
ARE VISION xLSTM EMBEDDED U -NETS MORE RELIABLE IN MEDICAL 3D IMAGE SEGMENTATION?

Pallabi Dutta

Machine Intelligence Unit
Indian Statistical Institute, Kolkata 700108, India
duttapallabi_r@isical.ac.in

Soham Bose

Department of Computer Science and Engineering
Jadavpur University, Kolkata 700032, India
sohamb.cse.ug@jadavpuruniversity.in

Swalpa Kumar Roy

Department of Computer Science and Engineering
Alipurduar Government Engineering
and Management College, West Bengal 736206, India
swalpa@agemc.ac.in

Sushmita Mitra

Machine Intelligence Unit
Indian Statistical Institute, Kolkata 700108, India
sushmita@isical.ac.in

ABSTRACT

The development of efficient segmentation strategies for medical images has evolved from its initial dependence on Convolutional Neural Networks (CNNs) to the current investigation of hybrid models that combine CNNs with Vision Transformers. There is an increasing focus on creating architectures that are both high-performance and computationally efficient, able to be deployed on remote systems with limited resources. Although transformers can capture global dependencies in the input space, they face challenges from the corresponding high computational and storage expenses involved. This paper investigates the integration of CNNs with Vision Extended Long Short-Term Memory (*Vision-xLSTM*)s by introducing the novel *U-VixLSTM*.

The *Vision-xLSTM* blocks capture temporal and global relationships within the patches, as extracted from the CNN feature maps. The convolutional feature reconstruction path upsamples the output volume from the *Vision-xLSTM* blocks, to produce the segmentation output. Our primary objective is to propose that *Vision-xLSTM* forms an appropriate backbone for medical image segmentation, offering excellent performance with reduced computational costs. The *U-VixLSTM* exhibits superior performance, compared to the state-of-the-art networks in the publicly available Synapse, ISIC and ACDC datasets. Code provided: <https://github.com/duttapallabi2907/U-VixLSTM>

1 Introduction

Artificial intelligence-driven medical image segmentation is one of the key cornerstones of modern healthcare, providing essential information for diagnosing, planning treatment, and monitoring patients. This task includes both volumetric and 2D imaging modalities. There are several challenges in accurately defining target regions from medical image data. These challenges stem from the complex characteristics of medical imaging data and variations in anatomical structures. Some common issues include ambiguous boundaries of target organs and pathologies, low contrast, overlapping structures, and inter- and intra-patient variability. Volumetric medical image data involves examining the spatial relationship between regions of interest (ROI) in numerous slices of volumetric data [1]. Consequently, it requires a substantial amount of computational resources for analysis. These challenges require the development of segmentation algorithms with a high degree of precision and accuracy at the output.

Deep learning is widely used in automated medical image segmentation, mainly due to its ability to extract underlying characteristics from input images with minimal human involvement and generalization to unseen samples [2]. The U -Net architecture [3], consisting of symmetric encoder-decoder structures with CNN, played a crucial role in revolutionizing the extensive use of deep learning in medical image segmentation. Hierarchical modeling of complex high-level patterns from low-level features and the integration of fine-grained spatial information with coarser abstract

features are the factors that are attributed to the success of the U -Net. Various well-known architectures have been developed to expand on their accomplishments. These include U -Net++ [4], V -Net [5], Attention U -Net [6] and U -Net 3+ [7]. Each of these introduces distinct modifications to improve performance and address specific difficulties inherent in medical image segmentation.

Combinations of CNNs and Transformers have been explored to combine their generic benefits to create a robust representation of target structures. Transformers overcome a significant drawback of CNNs through their self-attention mechanism; thereby, enabling them to effectively capture global relationships. In contrast, CNNs focus mainly on local patterns because of their limited field of view. TransUNet [8] pioneered the study of the impact of such a hybrid structure on medical image segmentation. It modeled the global structural dependencies in the intermediate feature volumes, produced from CNN layers, using the self-attention mechanism of Transformers [9]. This framework was also adopted into multiple segmentation tasks in the medical domain with the necessary modifications [10], [11] and [12]. Some other well-known hybrid CNN-Transformer architectures in this domain include UNETR [13], Swin UNETR [14], TransAttUNET [15], UNETR++ [16] and DS-TransUNet [17].

The self-attention mechanism, which is the driving force behind Transformers, suffers from the curse of quadratic complexity. This leads to a huge computational burden and memory requirement. Thereby, the applicability of Transformers gets limited in resource-constrained environments. Extended Long-Short Term Memory (xLSTM) [18] has recently emerged as a strong contender to Transformers in sequence modeling. It addresses the key limitations of Transformers with its inherent linear computational complexity $\mathcal{O}(n)$ and constant memory complexity $\mathcal{O}(1)$ w.r.t. the length of input sequences. *Vision-xLSTM* [19] pioneers the application of xLSTMs to computer vision tasks.

The efficiency of deep algorithms entails goodness of performance, both in terms of resource consumption and accuracy. This ensures the scalability of AI-driven algorithms in real-world problems. Clinical scenarios, with limited computing resources, require models that can accurately delineate target structures from medical data while constraining computational power and memory requirements. This is essential to guarantee sustainable and cost-effective healthcare solutions.

This need for computationally efficient and highly accurate segmentation algorithms motivated us to develop the new U - $VixLSTM$ model for medical image segmentation. Our approach integrates CNNs with *Vision-xLSTMs* for the first time (to the best of our knowledge) for segmentation. The architecture is based on the popular U -shaped framework reported in the literature [20], [21], [22], [23]. Our model is developed in two different versions: one for handling volumetric inputs and the other for handling 2D medical images. Our research contribution is summarized below.

- CNNs in the feature extraction path initially capture fine-grained textural information and local patterns corresponding to the target anatomical structures from the input image. The *Vision-xLSTM* blocks encode the global context within the intermediate output volumes, as obtained from the CNN layers.
- The feature reconstruction path upsamples the output from *Vision-xLSTM* blocks to produce the final segmentation output. Skip connections concatenate the feature volume from each level of the feature extraction path to the feature volume of the corresponding level of the feature reconstruction path, to build a robust representation of the target structures.
- Experimental results on two publicly available datasets, viz. *Synapse* [24], *ISIC* [25] and *ACDC* [26], illustrate the effectiveness of our model in terms of performance and utilization of computing resources.

The remaining sections of the paper are structured in the following manner. Section 2 discusses the existing literature. Section 3 presents the detailed description of the proposed architecture U - $VixLSTM$. The experimental results are illustrated in Section 4, along with a comparative study with state-of-the-art networks on publicly accessible datasets to validate the efficacy of U - $VixLSTM$. Finally, the article is concluded in Section 5.

2 Background Literature

TransUNet [8] introduced the pioneering approach to combine CNNs and Transformers to leverage their distinct benefits. The TransUNet framework was then improved [10] by incorporating an auxiliary decoder arm. A two-stage deep learning framework was used [11] for multi-organ segmentation from pelvic CT images. The initial phase involved the localization of organs utilizing a hybrid encoder framework, which comprised a convolutional stage followed by transformer modules. This output was subjected to several convolution operations.

Recent advances in attention mechanisms and transformer-based architectures have significantly improved the performance of medical image segmentation tasks. An efficient attention mechanism [27] was introduced to combine linear self-attention with frequency attention, using a Laplacian pyramid to selectively emphasize frequency contributions. This approach employs a fusion strategy to balance the shape and texture characteristics while improving overall

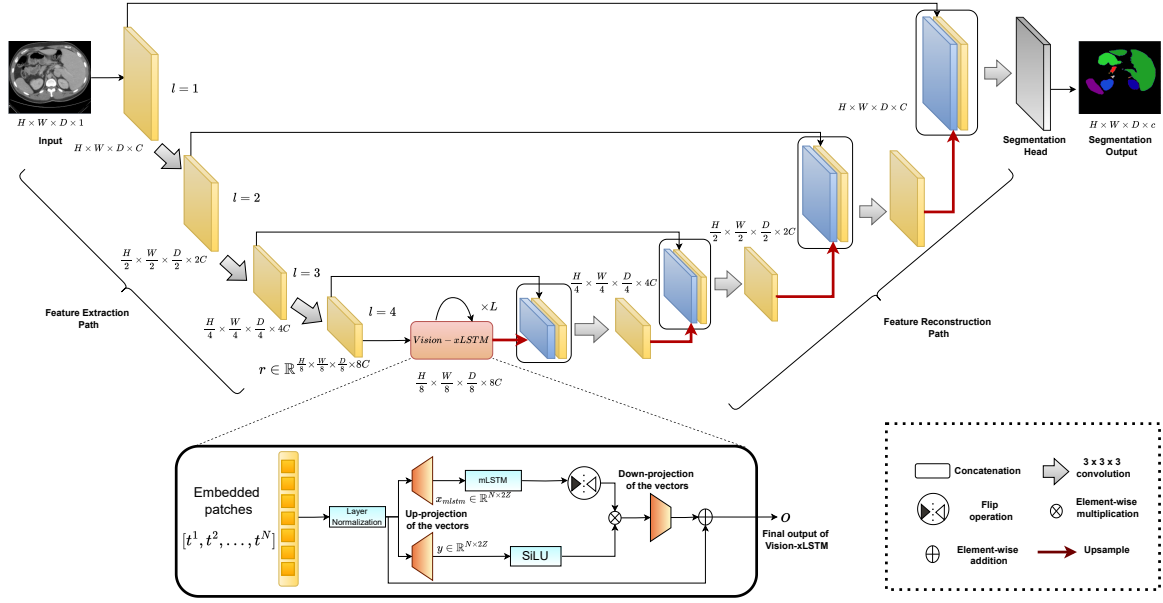


Figure 1: Architectural framework of $U\text{-VixLSTM}$ depicting the input processed by stacked layers of CNNs and $Vision\text{-}xLSTM$ blocks. The intermediate feature representation from the feature extraction path is upsampled through the feature reconstruction path to obtain the final segmentation output.

segmentation accuracy. UCTransNet [28] integrates a multi-scale channel cross-fusion transformer (CCT) and channel cross-attention (CCA) to enhance medical image segmentation. The CCT module fuses multiscale features through cross-attention mechanisms to capture long-range dependencies, while the CCA aids in refining Transformer and decoder feature fusion. This methodology has demonstrated a significant improvement in segmentation performance on multiple benchmarks. The TransAttU-Net [15], a Transformer-based attention-guided $U\text{-Net}$, integrates multilevel guided attention and multiscale skip connections for biomedical image segmentation. The Transformer Self-Attention and Global Spatial Attention mechanisms capture long-range dependencies and spatial relationships, while multiscale skip connections improve feature aggregation across semantic scales. This results in improved segmentation accuracy and consistency. An efficient Vision Transformer [29] was designed for medical image segmentation, featuring a Mixed Transformer module that includes Local-Global Self-Attention (LGG-SA) and External Attention (EA). While the LGG-SA captures local and global dependencies, using a focalized computation strategy, the EA exploits inter-sample correlations. This design reduced computational complexity, while improving segmentation accuracy, compared to traditional transformers. Recent advancements involve synergizing Mamba blocks with the shifting window approach of Swin UNETR, aiming to harness the benefits of State Space Models and Transformers [30].

Although the advanced methodologies listed can yield significant performance improvements, it is crucial to recognize their accompanying complexities. Complex operations often result in higher memory and computational demands. The concurrent matrix computations across various attention heads, typical of these methodologies, require considerable processing power. This may lead to delayed convergence during training, requiring extended training durations. They potentially impede scalability, particularly when processing high-resolution volumetric medical images. Incorporating auxiliary modules, although improving performance, inevitably increases the size and complexity of the model. This can present challenges in resource-constrained environments while increasing the risk of overfitting.

In this context, our study explores the hybridization of CNNs and $Vision\text{-}xLSTM$ s to address some of these limitations in medical image segmentation architectures. The proposed approach aims to achieve substantial performance improvements while preserving low computational complexity applicable to both volumetric and 2D contexts.

3 The Architecture

The structural framework of our proposed $U\text{-VixLSTM}$ model is depicted in Fig. 1. It follows the classic U -shaped framework, characterized by feature extraction and reconstruction pathways. Although the approach is outlined within the framework of 3D volumetric image processing, it can easily be modified for 2D images by reducing spatial dimension.

The feature extraction arm consists of CNN followed by *Vision-xLSTM* blocks in the bottleneck, which progressively reduce the size of the feature volumes to generate a high-level abstract representation of the image. The reconstruction path gradually builds the high-dimensional segmentation output, using the low-dimensional contextual representation from the preceding feature extraction path. The output of each convolution block in the feature extraction path is directed to its corresponding counterpart at the same level of the feature reconstruction path, through skip connections. This facilitates integration of feature maps that originate at various levels of abstraction. It ensures a judicious combination of the finer textural details from earlier convolution levels with the coarser semantic information of the deeper levels; thereby, resulting in enhanced context-sensitive predictions.

3.1 Feature extraction path

This path consists of key components, viz. CNNs for high-level feature learning and *Vision-xLSTM* for global dependencies.

3.1.1 High-level features

The volumetric input image $I \in \mathbb{R}^{H \times W \times D \times 1}$ is passed through a series of convolution layers to hierarchically construct an intermediate abstract and high-level representation of the image denoted by $r \in \mathbb{R}^{\frac{H}{8} \times \frac{W}{8} \times \frac{D}{8} \times 8C}$. Here H , W and D represent the height, width, and depth of the intermediate feature volume, respectively, with C corresponding to the number of channels.

Next, r is divided into $P \times P \times P$ non-overlapping patches. This is followed by the flattening of these patches into 1D vectors to yield a tokenized representation $t \in \mathbb{R}^{N \times (P^3 \frac{C}{4})}$. Here, $N = (\frac{H}{4} \times \frac{W}{4} \times \frac{D}{4}) / P^3$ denotes the number of flattened patches with dimension $P^3 \frac{C}{4}$. The flattened patches are then projected into a Z -dimensional embedding space, with learnable positional embeddings being added to preserve spatial location information. Mathematically, this is expressed as

$$p = [t^1 \mathbf{K}; t^2 \mathbf{K}; \dots; t^N \mathbf{K}] + K_{pos}, \quad (1)$$

where $\mathbf{K} \in \mathbb{R}^{(P^3 \frac{C}{4} \times Z)}$ is the projection matrix and $\mathbf{K}_{pos} \in \mathbb{R}^{N \times Z}$ is the position embedding matrix. $p \in \mathbb{R}^{N \times Z}$ represents the flattened patches.

3.1.2 Global dependencies

The projected patches are processed by a stack of *Vision-xLSTM* (ViL) [19] blocks. The structure comprises alternating ViL blocks, with the even-numbered blocks handling patch tokens from the top left to the bottom right, and the odd-numbered ones from the bottom right to the top left. Such bidirectional processing enables ViL blocks to capture robust global dependencies in the input.

The flattened patches, after normalization, are projected onto an embedding space to increase their dimension by a factor of 2. These expanded embeddings are divided into two paths, $x_{mlstm} \in \mathbb{R}^{N \times 2Z}$ and $y \in \mathbb{R}^{N \times 2Z}$ as shown in the detailed representation of the ViL block in Fig. 1. The x_{mlstm} undergoes a 1D causal convolution with SiLU activation [31]. The intermediate result ($\mathbf{X} \in \mathbb{R}^{N \times 2Z}$) is then mapped onto query vector (q), key vector (k) and value (v) vectors, which are similar to the vectors used in the Transformer architecture. These vectors are transmitted to the mLSTM cell. Here, the mLSTM sublayer comprises n parallel attention heads, each equipped with a matrix memory cell. The generation of query, value and keys is mathematically represented as

$$\mathbf{Q} = \mathbf{XW}_Q^T, \quad \mathbf{K} = \mathbf{XW}_K^T, \quad \mathbf{V} = \mathbf{XW}_V^T, \quad (2)$$

where $\mathbf{Q} \in \mathbb{R}^{N \times 2Z}$, $\mathbf{K} \in \mathbb{R}^{N \times 2Z}$, $\mathbf{V} \in \mathbb{R}^{N \times 2Z}$ are the query, key and value matrices, respectively. Here, $W_Q \in \mathbb{R}^{2Z \times 2Z}$, $W_K \in \mathbb{R}^{2Z \times 2Z}$, $W_V \in \mathbb{R}^{2Z \times 2Z}$, are learnable weight matrices to generate the query, key, and value vectors.

First the input and forget gate pre-activations, $\tilde{i} \in \mathbb{R}^{N \times 2Z}$ and $\tilde{f} \in \mathbb{R}^{N \times 2Z}$ are calculated by linearly projecting the concatenated \mathbf{Q} , \mathbf{K} and \mathbf{V} matrices as

$$\tilde{i} = (\mathbf{W}^I)^T [\mathbf{Q}, \mathbf{K}, \mathbf{V}] + \mathbf{B}, \quad (3)$$

$$\tilde{f} = (\mathbf{W}^F)^T [\mathbf{Q}, \mathbf{K}, \mathbf{V}] + \mathbf{B}. \quad (4)$$

Here, $\mathbf{B} \in \mathbb{R}^{N \times 2Z}$ is the bias matrix. $\mathbf{W}^I, \mathbf{W}^F \in \mathbb{R}^{6Z \times 2Z}$ are the projection matrices for \tilde{i} and \tilde{f} respectively. The pre-activations are used to derive the gate decay matrix $\mathbf{D} \in \mathbb{R}^{N \times 2Z}$ using

$$\mathbf{D} = \tilde{i} \oplus \text{lo}(\tilde{f}), \quad (5)$$

with $l\sigma$ denoting the log-sigmoid activation function and \oplus represents the element-wise addition operation. The decay matrix \mathbf{D} is further stabilized to ensure that the subsequent exponentiation of \mathbf{D} produces a stable output. The final gate decay matrix output $\hat{\mathbf{D}} \in \mathbb{R}^{N \times 2Z}$ is expressed as

$$\hat{\mathbf{D}} = \exp(\mathbf{D}), \quad (6)$$

with \exp representing exponentiation. $\hat{\mathbf{D}}$ regulates the flow of information to the memory matrix. Vectors \mathbf{Q} and \mathbf{K} undergo a dot product multiplication to generate attention scores $\mathbf{S} \in \mathbb{R}^{N \times N}$, analogous to the self-attention mechanism of Transformers. A causal mask $\mathbf{M} \in \mathbb{R}^{N \times N}$ guarantees that attention is directed exclusively from the previous patch to the current patch. This is computed as

$$\mathbf{S} = \text{Softmax}\left(\frac{\mathbf{Q}\mathbf{K}^\top}{\sqrt{d}} + \mathbf{M}\right). \quad (7)$$

The attention score matrix is multiplied by $\hat{\mathbf{D}}$ to get the combination matrix $\mathbf{C} \in \mathbb{R}^{N \times 2Z}$. We have

$$\mathbf{C} = \mathbf{S}^\top \hat{\mathbf{D}}. \quad (8)$$

Finally, the updated cell state $\tilde{h}_t \in \mathbb{R}^{N \times 2Z}$ is computed as

$$\tilde{h}_t = \mathbf{C} \otimes \mathbf{V}. \quad (9)$$

Here \otimes represents element-wise multiplication operation. The embedding y , generated from the second path, is multiplied by \tilde{h}_t followed by a down-projection of the final output o onto the Z -dimensional embedding space. This is evaluated as

$$o = (\mathbf{W}^\mathbf{D})^\top (y \otimes \tilde{h}_t), \quad (10)$$

with $\mathbf{W}^\mathbf{D} \in \mathbb{R}^{2Z \times Z}$ being the projection matrix.

3.2 Feature reconstruction path

A trilinear upsampling operation τ is employed, at every level l , to increase the spatial dimension of the feature maps obtained from the previous level $l + 1$. This helps align the spatial dimensions of the feature maps with those received from the corresponding level l of the feature extraction path. The upsampled feature map at level l is expressed as

$$\mathbf{U}_l = \tau(\mathbf{F}_{l+1}), \quad (11)$$

where \mathbf{F}_{l+1} is the output volume from level $l + 1$.

The upsampled feature map \mathbf{U}_l is then concatenated with the feature volume from the corresponding level l of the feature extraction path, denoted as \mathbf{E}_l . The concatenated feature volume at level l is given by

$$\mathbf{C}_l = \text{Concat}(\mathbf{U}_l, \mathbf{E}_l). \quad (12)$$

It is then convolved to yield the output volume \mathbf{R}_l at level l of the feature reconstruction path, as

$$\mathbf{R}_l = \text{Conv}_{3 \times 3 \times 3}(\mathbf{C}_l). \quad (13)$$

The training procedure for *U-VixLSTM* is described in Algorithm 1.

4 Experimental Details

This section describes the loss functions and performance metrics used for the evaluation, details of the datasets used, and the experimental results.

4.1 Loss function and metrics

A loss function combination of Dice $\mathcal{L}_{dice} = \gamma - \sum_{\gamma=1}^c \left(\frac{2 \sum_{i=1}^T \hat{z}_{\gamma,i} z_{\gamma,i} + \mu}{\sum_{i=1}^T \hat{z}_{\gamma,i} + z_{\gamma,i} + \mu} \right)$ [5] and Categorical Cross Entropy [32] $\mathcal{L}_{cce} = -\frac{1}{T} \sum_{i=1}^T \sum_{\gamma=1}^c z_{\gamma,i} \log(\hat{z}_{\gamma,i})$, was employed. Here, c represented the total number of classes to be predicted, $\hat{z}_{\gamma,i}$ and $z_{\gamma,i}$ corresponded to the predicted and ground truth values (respectively) for the i^{th} voxel for class γ , T denoted the total number of voxels in the input, and μ was the additive smoothing parameter used to overcome division-by-zero errors. The composite loss function \mathcal{L} was expressed as

$$\mathcal{L}(\{\hat{\rho}, \rho\}; \Gamma) = \mathcal{L}_{dice}(\{\hat{\rho}, \rho\}, \Gamma) + \mathcal{L}_{cce}(\{\hat{\rho}, \rho\}, \Gamma), \quad (14)$$

Algorithm 1 Training Process for *U-VixLSTM*

Input: Training dataset $\Delta = \{(I_j, O_j)\}_{j=1}^m$, Patch size P , Embedding dimension Z , Number of *Vision-xLSTM* blocks L , Projection matrix K , Positional embedding K_{pos} , learning rate ϵ and number of iterations ι

Output: Segmentation output $\{\hat{O}_j\}_{j=1}^m$

```
1: Initialize weights  $\Omega$ 
2: while iterations  $\leq \iota$  do
3:   /* Feature Extraction Path */
4:   for  $l = 1$  to  $x$  do /* Iterating through different levels of feature extraction path */
5:      $E_l = Conv(E_{l-1})$  /* Apply convolution */
6:      $E_l = ReLU(E_l)$ 
7:      $E_l = MaxPool(E_l)$ 
8:   end for
9:    $r \leftarrow E_x$  /* Intermediate feature representation  $r$  from a series of convolution blocks at level  $x$  */
10: /* Divide  $r$  into  $N = \frac{HWD}{P^3}$  patches of size  $P^3$  */
11:    $conv \leftarrow Conv3D$  (filters =  $\frac{HWD}{P^3}$ , kernel size =  $(P, P, P)$ )
12:    $patches = conv(r)$ 
13:   Flatten patches into tokens  $t$ 
14:   /* Project tokens to embedding space  $Z$  */
15:    $p \leftarrow []$ 
16:   for  $i = 1$  to  $N$  do
17:      $p.append(t_i * K)$ 
18:   end for
19:    $p \leftarrow p + K_{pos}$ 
20:   for  $i = 1$  to  $L$  do /* Apply Vision-xLSTM Blocks */
21:     Compute  $Q^i, K^i, V^i$  matrices and attention scores  $S^i$  with a causal mask
22:     Update memory state  $\tilde{h}_t^i$  and obtain output  $o^i$ 
23:   end for
24:   /* Feature Reconstruction Path */
25:   for  $l = x - 1$  to  $1$  do
26:      $U_l \leftarrow \tau(F_{l+1})$ 
27:      $C_l \leftarrow Concat(U_l, E_l)$ 
28:      $R_l \leftarrow Conv(C_l)$ 
29:   end for
30:    $\hat{O} \leftarrow Conv_{1 \times 1 \times 1}(R_1)$ 
31:   Compute loss  $\mathbf{L}(\{O, \hat{O}\})$ 
32:    $\Omega' \leftarrow \Omega - \epsilon \frac{\partial \mathbf{L}}{\partial \Omega}$  /*Weight updation*/
33: end while
```

with Γ denoting the model parameters, $\hat{\rho}$ and ρ symbolizing predicted segmentation map and ground truth, respectively.

The Dice Score Coefficient (*DSC*), Intersection-Over-Union (*IoU*), and 95% Hausdorff Distance (*HD95*) were the performance metrics used to evaluate the segmentation output.

Experimental Setup: The PyTorch and MONAI frameworks were used to implement and train *U-VixLSTM* in Python 3.9 on an NVIDIA RTX A6000 GPU with 48GB of RAM. AdamW Optimizer was used, with a learning rate of 1e-4 and a weight decay of 1e-5.

4.2 Datasets

The data set *Synapse* comprises 30 CT volumes, with sizes ranging from $512 \times 512 \times 85$ to $512 \times 512 \times 198$. CT volumes are manually annotated by experts in the field to highlight the different abdominal organs. A model is trained to segment nine distinct organs of the abdominal cavity *viz.* spleen, left kidney, right kidney, liver, gall bladder, pancreas, stomach, right adrenal gland, and left adrenal gland. The spleen, liver, and stomach are classified as larger organs, while the kidneys, gall bladder, pancreas, and adrenal glands are smaller in size. The CT volumes were divided into training and test sets, with 80% used for training and the remaining 20% used for testing to evaluate the generalization performance of the model. The voxel intensities were restricted between -170 HU and 250 HU, followed by normalization of the intensity to the range of [0,1]. Data augmentation was effective in expanding the size of the training dataset.

The *ISIC* dataset contains dermoscopic images with pixel values $\in [0, 255]$. These images have been curated by the International Skin Imaging Collaboration (ISIC) for the study of skin cancer. The training dataset consists of 2000

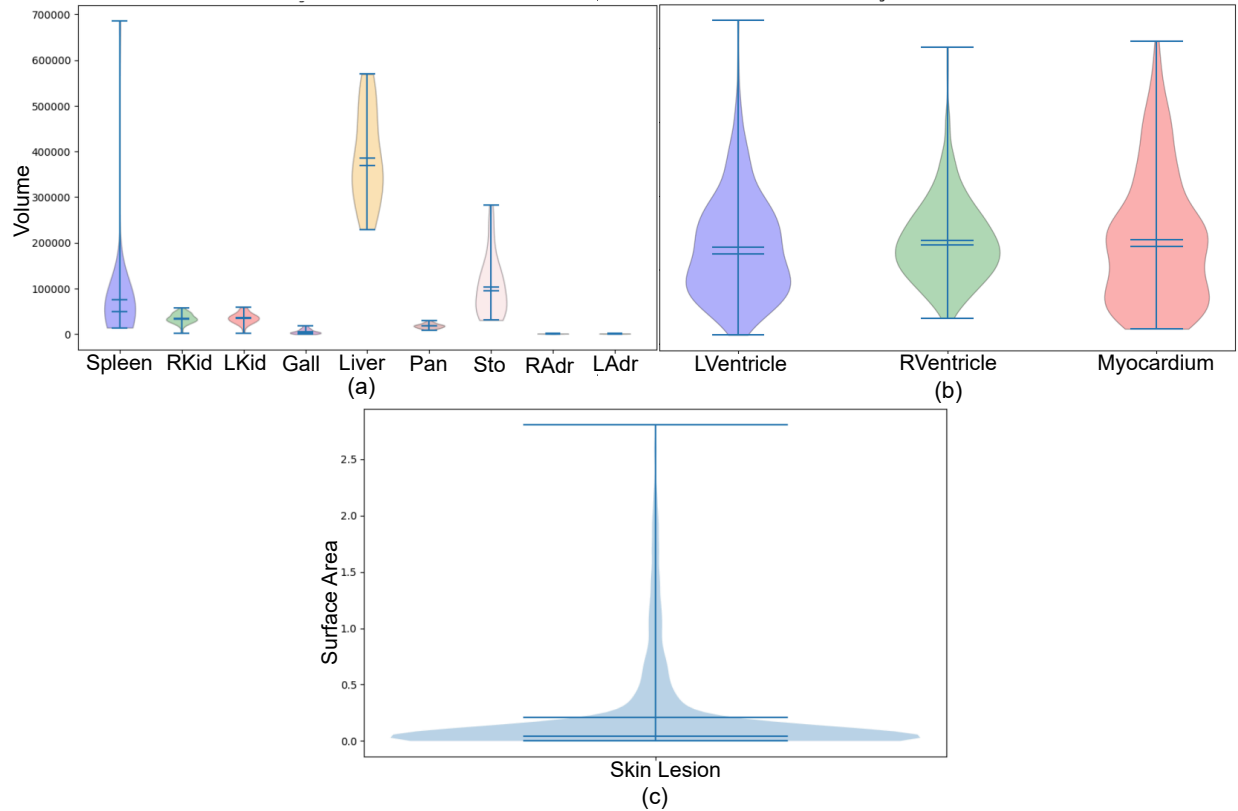


Figure 2: Distribution of (a) various abdominal organs, (b) skin lesion surface area, and (c) cardiac anatomical structures, among different patients in the *Synapse*, *ISIC*, and *ACDC* datasets, respectively.

images with corresponding ground truth masks prepared by domain experts. The test set consists of 600 images. The value of pixel 0 in the ground truth mask corresponds to the background region, whereas the value of pixel 255 corresponds to the lesion region. The input images and their corresponding masks were normalized to the pixel values $\in [0, 1]$. The training data was augmented by rotation and random cropping transformation.

The dataset *ACDC* consists of 150 volumes of chest magnetic resonance images for automated cardiac diagnosis. Magnetic resonance volumes were obtained from the University Hospital of Dijon, France. The experts prepared the corresponding ground truth volumes, which have segmentations for the right ventricle (RV), left ventricle (LV), and myocardium. Volumes were pre-processed analogously to that of the *Synapse* dataset.

Fig. 2 illustrates the distribution of abdominal and cardiac organ volumes, as well as the surface area of skin lesions, between patients in the three datasets. The plots demonstrate substantial evidence of inter-patient variability across the datasets, indicating significant differences in the sizes of various organs or lesion areas among patients. Quite a significant difference in morphology is evident in the spleen, liver, and stomach, as shown in Fig. 2(a), in the cardiac organs of Fig. 2(b), and in the total surface area of the lesion illustrated in Fig. 2(c), as attributed to long tails and broader distributions. The median values indicate significant heterogeneity in the average volumes of the various abdominal organs. The liver exhibits the largest average volume, followed by the stomach and spleen. The adrenal gland exhibits the lowest average volume among the glands. The diverse sizes of target structures hinder the ability of the model to generalize across datasets. Fig. 2(c) illustrates a right-skewed distribution of the surface area of the lesions. This suggests that patients generally have smaller lesion areas compared to larger ones. This may indicate a class imbalance within the dataset.

The volumetric samples of *Synapse* and *ACDC* are processed by the 3D version of *U-VixLSTM* while the 2D version is trained using the samples from *ISIC* dataset.

Table 1: Comparison of different variants of *U-VixLSTM*, with increasing number of *Vision-xLSTM* blocks ($\times L$) and increasing number of convolution layers, on *Synapse* data. Best results and the selected model configuration are highlighted in **bold**.

Ablations	Model Variants	mDSC	mIoU	mHD95
# <i>Vision-xLSTM</i> blocks	x 6	0.8318	0.7323	4.8
	x 12	0.8289	0.7286	8.57
	x 18	0.8201	0.7189	4.34
	x 24	0.8299	0.728	19.05
# Convolution Layers	3	0.8143	0.7114	5.48
	4	0.8318	0.7323	4.8
	5	0.8314	0.7315	4.85

Table 2: Comparison with state-of-the-art models, on multi-organ segmentation (*Synapse*) dataset. The best results are highlighted in **bold**.

Model	DSC										IoU Mean	HD95 Mean
	Spleen	Right kidney	Left kidney	Gall Bladder	Liver	Pancreas	Stomach	Right Adrenal	Left Adrenal	Mean		
<i>U-Net</i> [3]	0.9112	0.9007	0.9181	0.5645	0.9572	0.6967	0.78	0.616	0.5872	0.7702	0.6667	38.83
<i>V-Net</i> [5]	0.8874	0.9251	0.9244	0.5858	0.9487	0.7511	0.7953	0.6004	0.4497	0.7631	0.6537	25.29
<i>U-Net++</i> [4]	0.9118	0.9196	0.8905	0.6921	0.9524	0.7536	0.7869	0.5245	0.1032	0.7261	0.6254	55.27
Attention <i>U-Net</i> [6]	0.9109	0.877	0.872	0.5835	0.9585	0.5566	0.7846	0.5991	0.5398	0.7424	0.6262	51.61
<i>U-Net</i> + EfficientNet-b0 [33]	0.8541	0.8919	0.8804	0.637	0.9077	0.5018	0.7097	0.6048	0.5195	0.723	0.6056	67.47
<i>U-Net</i> + EfficientNet-b1 [33]	0.7414	0.8059	0.8256	0.55	0.9019	0.5416	0.616	0.525	0.5035	0.6679	0.5539	75.85
<i>U-Net</i> 3+ [7]	0.8736	0.9229	0.8584	0.6659	0.9383	0.6823	0.7259	0.5657	0.4764	0.7455	0.6254	54.43
SwinUNet [14]	0.9482	0.93	0.9245	0.7617	0.9622	0.8046	0.8059	0.689	0.6159	0.8269	0.7261	13.99
UNETR [13]	0.8951	0.9055	0.895	0.5274	0.9461	0.6668	0.7847	0.5268	0.4978	0.7384	0.6284	26.94
TransUNET [8]	0.852	0.8828	0.785	0.7608	0.587	0.7218	0.8773	0.5876	0.4672	0.7246	0.6679	36.81
TransAttUNET [15]	0.9045	0.8761	0.916	0.4958	0.9408	0.5997	0.6682	0.6559	0.5948	0.7391	0.658	15.82
Swin UMamba [30]	0.8778	0.9037	0.9112	0.4206	0.9161	0.6238	0.6527	0.589	0.5617	0.7174	0.6334	20.1
UNETR++ [16]	0.8061	0.8050	0.8201	0.5208	0.8868	0.5249	0.5576	0.589	0.4577	0.6631	0.534	8.61
DS-TransUNET [17]	0.4965	0.6113	0.5252	0.5397	0.679	0.5295	0.5857	0.5745	0.5266	0.5631	0.4644	14.79
<i>U-VixLSTM</i>	0.95	0.9371	0.9366	0.8104	0.9635	0.7878	0.8304	0.6709	0.6458	0.8318	0.7286	4.8

4.3 Results

Table 1 presents an ablation study on *Synapse* data, demonstrating the impact of different numbers (L) of *Vision-xLSTM* blocks and a varying number of convolution layers along the feature extraction path. The average scores DSC , $HD95$, and IoU are reported for the different organs. The ablation study reflects the trade-off between the complexity of the model and its performance. Increasing the number of convolution layers from three to four shows a significant gain in metric scores. However, the performance saturates on further increase in the number of layers. The best DSC and IoU values were observed for the lowest number of *Vision-xLSTM* blocks. The $HD95$ scores showed minimal improvement with 18 *Vision-xLSTM* blocks, compared to six. This implies that the lower computational and memory requirements of *U-VixLSTM* resulted in higher efficiency w.r.t. DSC and IoU . However, a slightly deeper architecture may provide small improvements in accurately defining object boundaries with increased computational overhead. It was seen that a model with 6 *Vision-xLSTM* blocks attained an offset between efficient performance and low computational complexity.

The performance of our *U-VixLSTM* was next compared with that of the state-of-the-art (SOTA) algorithms in the literature in terms of metrics DSC , IoU , $HD95$ on *Synapse*, *ISIC* and *ACDC* datasets. Table 2 presents a comprehensive breakdown of performance in the different organs (in *Synapse* data) in the context of DSC . The average results for $HD95$ and IoU are provided for the nine abdominal organs. *U-VixLSTM* is found to outperform other SOTA, with respect to the mean DSC , IoU and $HD95$, with scores of 83.18%, 72.86%, and 4.8, respectively. Our proposed *U-VixLSTM* demonstrated superior performance in generating the highest DSC values for the segmentation of larger organs (such as the spleen, liver) and smaller organs (such as the kidneys, pancreas, gall bladder and left adrenal gland). Performance remained stable, despite the reduction in organ size, as indicated by the consistently high DSC scores observed in smaller and larger organs. This illustrates the robustness of our model in utilizing acquired knowledge on anatomical structures with varying shapes and sizes. It is found to precisely identify and define the target areas possessing unique structures.

Fig. 3 shows the sample segmentation output of *U-VixLSTM* and other architectures, such as Swin-UNETR, UNETR, *V-Net*, and TransAttUNet, on the *Synapse* dataset. It is evident that the *U-VixLSTM* model demonstrates a significantly higher level of similarity to the ground truth, compared to the maps produced by these other baseline models. The

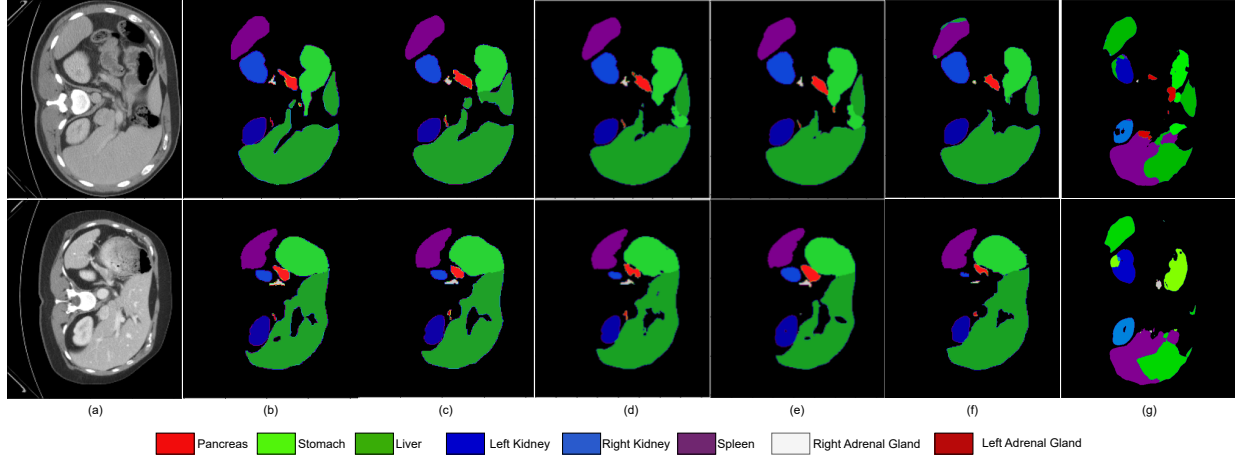


Figure 3: Comparative performance of *U-VixLSTM* and other baseline architectures, on the *Synapse* dataset, through sample segmentation maps. The (a) input CT image, (b) corresponding ground truth, with the respective output from (c) *U-VixLSTM*, (d) Swin UNETR, (e) UNETR, (f) *V-Net*, and (g) TransAttUNet.

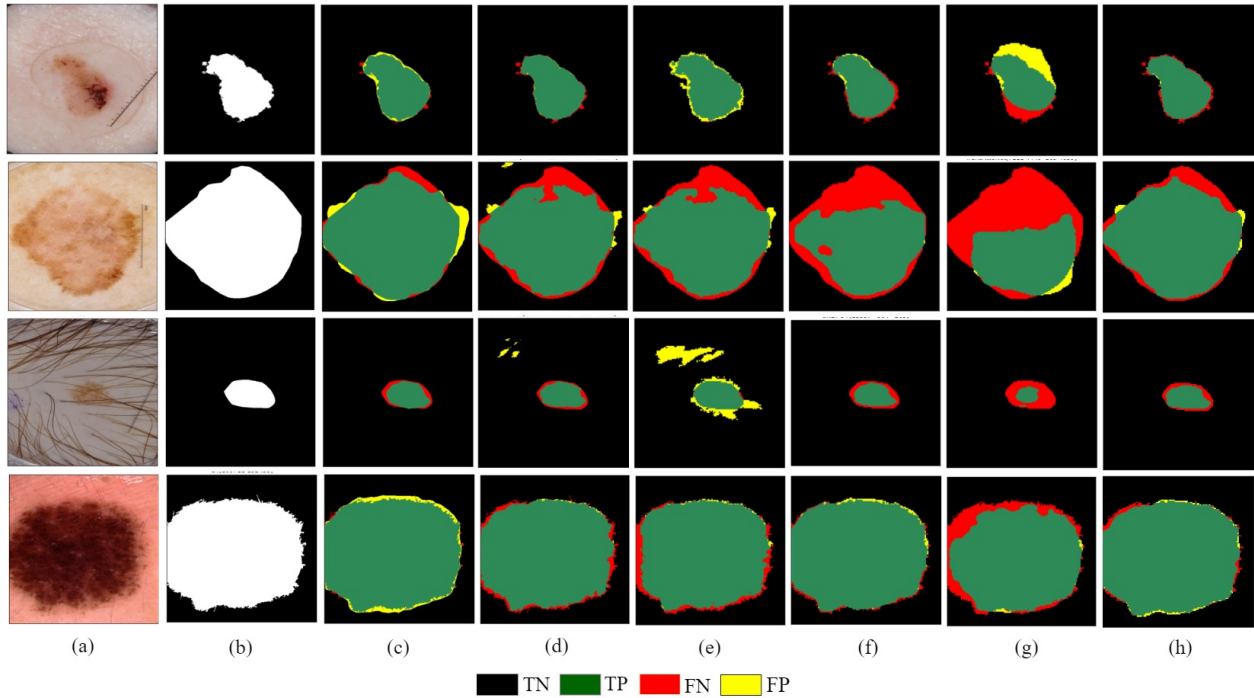


Figure 4: Comparative performance of *U-VixLSTM* and other baseline architectures, on the *ISIC* dataset, through sample segmentation maps. The (a) input dermoscopic image, (b) corresponding ground truth, with the respective output from (c) *U-VixLSTM*, (d) Swin UNETR, (e) UNETR, (f) *U-Net 3+*, (g) TransAttUNet, and (h) DS-TransUNet.

results of the Swin UNETR and UNETR models show *FP* regions corresponding to the stomach, in the first row of Figs. 3 (d) and (e). The result of *V-Net* in the upper row of Fig. 3 (f) demonstrates that pixels associated with the boundary areas of the spleen were incorrectly classified. It also demonstrates a lack of precision in identifying the anatomical regions associated with the left adrenal gland, along with a lack of division of the right adrenal gland. The segmentation maps obtained from TransAttUNet exhibit their limited capacity to learn complex representations corresponding to multiple organs, with varying shapes and sizes.

Fig. 4 represents the sample segmentation output, as predicted by *U-VixLSTM* and other baseline models on the *ISIC* dataset. The prediction made by our *U-VixLSTM* exhibits higher accuracy and precision in relation to the ground truth

Table 3: Comparison with state-of-the-art models on the *ISIC* dataset. The best results are highlighted in **bold**.

Model	DSC	IOU	HD95
<i>U</i> -Net	0.8065	0.7197	74.72
Attention <i>U</i> -Net	0.7798	0.6845	87.13
<i>U</i> -Net + EfficientNet-b0	0.8222	0.7315	12.32
<i>U</i> -Net + EfficientNet-b1	0.812	0.7176	13.44
<i>U</i> -Net ++	0.8074	0.7057	13.37
<i>U</i> -Net 3+	0.7732	0.6772	14.77
Swin UNETR	0.8187	0.7289	61.06
TransUNET	0.7012	0.6086	90.32
UNETR	0.7601	0.6495	19.04
TransAttUNet	0.758	0.661	82.22
DS-TransUNET	0.8212	0.7304	12.50
Swin UMamba	0.8237	0.7330	56.41
<i>U-VixLSTM</i>	0.85	0.7611	11.31

Table 4: Comparison with state-of-the-art models on the *ACDC* dataset. The best results are highlighted in **bold**.

Model	DSC			mIOU	mHD
	LVentricle	RVentricle	Myocardium		
UNet	0.7869	0.7956	0.891	0.713	7.29
V-Net	0.7273	0.6969	0.8108	0.6145	6.34
UNet++	0.6155	0.6828	0.8302	0.5693	54.35
Attention U-Net	0.7087	0.7637	0.8689	0.6568	8.32
UNet with EfficientNet-b0 backbone	0.6236	0.5314	0.7069	0.5219	104.65
UNet with EfficientNet-b1 backbone	0.6543	0.5217	0.7299	0.5026	98.27
UNet 3+	0.6903	0.6412	0.7355	0.5463	149.64
SwinUNet	0.8059	0.7741	0.8838	0.7076	6.02
UNETR	0.7052	0.6845	0.8316	0.6049	9.84
TransUNET	0.6398	0.7692	0.8714	0.6581	6.93
TransAttUNET	0.6338	0.742	0.8819	0.6432	95.35
Swin UMamba	0.664	0.7907	0.8699	0.672	5.45
DS-TransUNET	0.6396	0.7688	0.8654	0.654	5.32
UNETR++	0.7026	0.6977	0.8264	0.654	5.32
<i>U-VixLSTM</i>	0.868	0.8345	0.9104	0.777	5.07

masks, compared to the maps generated by the other baseline models. The sample outputs from the other state-of-the-art architectures mostly contain undersegmented or oversegmented regions. For example, along rows 2 and 3, the baseline models exhibit a significant amount of *FN* and *FP* regions; our *U-VixLSTM*, on the other hand, has a visually higher proportion of *TP* regions and fewer *FP* and *FN* pixels. This indicates that these other models had difficulty accurately identifying the boundaries of the target region(s). The quantitative results, presented in Table 3, demonstrate (for our *U-VixLSTM*) the highest values of *DSC* and *IoU* along with the lowest *HD95* metric score. This corroborates the qualitative observation of the enhanced segmentation accuracy of our proposed model.

Table 4 presents a comprehensive analysis of performance in different organs in the dataset *ACDC* concerning the *DSC* value. The average results for HD95 and IoU are tabulated for various cardiac organs. *U-VixLSTM* has outperformed baselines, attaining a *DSC* value of 86. 8%, 83. 45% and 91. 04% for the three distinct cardiac organs, respectively. The mean IoU is 77. 7%, exceeding the best baseline by approximately 6%. Fig. 5 shows sample segmentation maps generated by *U-VixLSTM* along with various baseline methods. The visual representation illustrates the higher-quality outputs generated by our proposed methods relative to established baselines. Instances of mis-segmentations and false positive pixels are evident in the sample maps from Swin UNETR, UNETR, and V-Net, as illustrated in Fig. 5(d)-(g).

Fig. 6 illustrates sample feature maps obtained from the convolution and *Vision-xLSTM* modules within the feature extraction pathway. The maps visualize the representations acquired by the two modules of the proposed network in

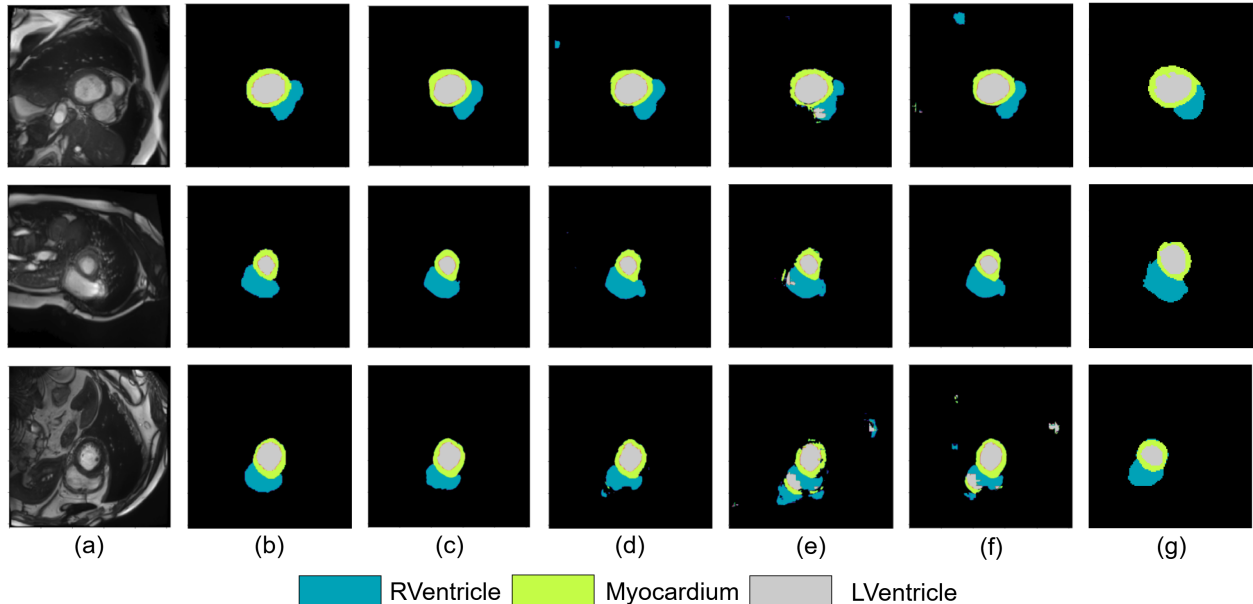


Figure 5: Comparative performance of *U-VixLSTM* and other baseline architectures, on the *ACDC* dataset, through sample segmentation maps. The (a) input CT image, (b) corresponding ground truth, with the respective output from (c) *U-VixLSTM*, (d) Swin UNETR, (e) UNETR, (f) *V-Net*, and (g) TransAttUNet

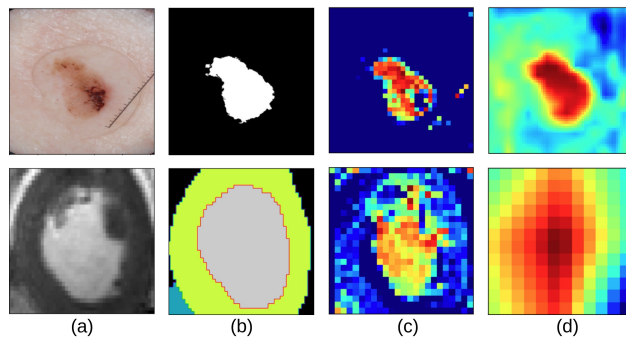


Figure 6: Visualization of (a) input image, (b) ground truth, and feature maps from (c) CNN and (d) ViL blocks of the feature extraction path.

relation to the target structures, as specified in the ground truth. The shades of red represent the regions of strongest activation where the model allocates the majority of its attention, whereas the shades of dark blue signify the lowest activation levels. This visualization helps us observe the areas in the input image that are the most important to the model to define the target structure.

The enhanced performance of *U-VixLSTM* in various modalities is due to its effective capture of local and contextual information. The CNN blocks initially hierarchically extract fine-grained details, such as edges and local patterns. The *Vision-xLSTM* blocks at the bottleneck connect distant sections of intermediate feature maps, effectively capturing the overall relationships and dependencies among various parts of target structures that have different shapes and sizes. This effectively constructs global contextual information. Incorporating skip connections that merge feature maps from the extraction path with the corresponding levels of the reconstruction path facilitates the localization of anatomical structures. Consequently, *Vision-xLSTMs* enhance the feature extraction process by acquiring superior feature representations while maintaining lower computational costs relative to baseline methods.

Fig. 7 provides a graphical analysis of the parameter count, Tera Floating point Operations (TFLOPs), and memory size on disk, of our *U-VixLSTM* compared to that of other baseline architectures under consideration. The analysis shows that *U-VixLSTM* has the lowest number of parameters and TFLOPs (floating point operations per second) compared to the other SOTA. This reiterates our claim about the superior computational efficiency of the proposed model. Hence, it demonstrates potential for deployment in resource-constrained environments.

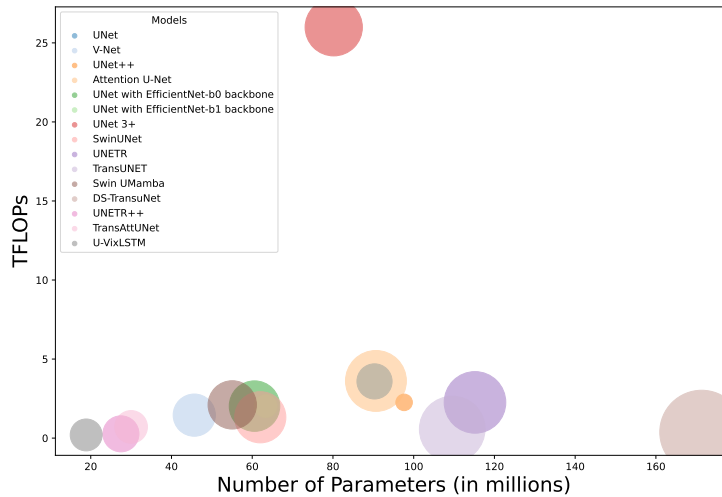


Figure 7: Comparison between state-of-the-art models w.r.t number of parameters (in millions), TFLOPs, and memory size (in MB). Bubble size is indicative of model size.

5 Conclusions and Discussion

This research introduced the first integration of CNNs with *Vision-xLSTMs* for image segmentation (specifically, medical image segmentation), using the widely used *U*-shaped framework. CNNs acquired intricate spatial and textural information from the input image. The *Vision-xLSTMs* captured both global and temporal relationships inside the patches, derived from the feature volume produced by CNNs; thus learning a robust representation for the target structures.

The superiority of our model *U-VixLSTM* can be attributed to various factors. The incorporation of CNNs with *Vision-xLSTM* allowed the model to effectively capture both local and global contextual information, which was essential to achieve precise segmentation. Furthermore, the utilization of *Vision-xLSTM* enhanced the efficiency of the model in terms of the total number of parameters and FLOPs, compared to other hybrid CNN transformer methods. This has substantial implications for clinical practice by increasing the accessibility of our model in a scenario with limited resources. This can potentially lead to an expedited and effective identification of medical conditions, decision-making for treatment, and providing guidance during surgical procedures.

Acknowledgement

This work was supported by the J. C. Bose National Fellowship, grant no. JCB/2020/000033 of S. Mitra.

References

- [1] G. H. Choi, J. Yun, and *et al.*, “Development of machine learning-based clinical decision support system for hepatocellular carcinoma,” *Scientific Reports*, vol. 10, p. 14855, 2020.
- [2] X. Chen, X. Wang, and *et al.*, “Recent advances and clinical applications of deep learning in medical image analysis,” *Medical Image Analysis*, vol. 79, p. 102444, 2022.
- [3] O. Ronneberger, P. Fischer, and *et al.*, “*U*-Net: Convolutional networks for biomedical image segmentation,” in *Proceedings of the International Conference on Medical Image Computing and Computer Assisted Intervention (MICCAI)*, pp. 234-241, Springer, 2015.
- [4] Z. Zhou, R. Siddiquee, and *et al.*, “*U*-Net++: A nested *U*-Net architecture for medical image segmentation,” in *Deep Learning in Medical Image Analysis and Multimodal Learning for Clinical Decision Support*, pp. 3-11, Springer, 2018.

- [5] F. Milletari, N. Navab, and *et al.*, “V-Net: Fully convolutional neural networks for volumetric medical image segmentation,” in *Proceedings of Fourth International Conference on 3D vision (3DV)*, pp. 565-571, IEEE, 2016.
- [6] O. Oktay, J. Schlemper, and *et al.*, “Attention U-Net: Learning where to look for the pancreas,” in *Proceedings of the Medical Imaging with Deep Learning*, pp. 1–10, 2018.
- [7] H. Huang, L. Lin, and *et al.*, “U-Net 3+: A full-scale connected U-Net for medical image segmentation,” in *Proceedings of IEEE International Conference on Acoustics, Speech and Signal Processing (ICASSP)*, pp. 1055–1059, IEEE, 2020.
- [8] J. Chen, Y. Lu, and *et al.*, “TransUNet: Transformers make strong encoders for medical image segmentation,” *arXiv preprint arXiv:2102.04306*, 2021.
- [9] A. Vaswani, N. Shazeer, and *et al.*, “Attention is all you need,” vol. 30, 2017.
- [10] J. Cheng, J. Liu, and *et al.*, “A fully automated multimodal MRI-based multi-task learning for glioma segmentation and IDH genotyping,” *IEEE Transactions on Medical Imaging*, vol. 41, pp. 1520–1532, 2022.
- [11] R. Pemmaraju, D. Y. Song, and *et al.*, “Cascaded neural network segmentation pipeline for automated delineation of prostate and organs at risk in male pelvic CT,” in *Proceedings of Medical Imaging 2023: Image Processing*, vol. 12464, pp. 311–318, SPIE, 2023.
- [12] B. Wang, F. Wang, and *et al.*, “Multiscale TransUNet++: Dense hybrid U-Net with transformer for medical image segmentation,” *Signal, Image and Video Processing*, vol. 16, pp. 1607–1614, 2022.
- [13] A. Hatamizadeh, Y. Tang, and *et al.*, “UNETR: Transformers for 3D medical image segmentation,” in *Proceedings of the IEEE/CVF Winter Conference on Applications of Computer Vision*, pp. 574–584, 2022.
- [14] A. Hatamizadeh, V. Nath, and *et al.*, “Swin UNETR: Swin transformers for semantic segmentation of brain tumors in MRI images,” in *Proceeding of International MICCAI Brainlesion Workshop*, pp. 272–284, Springer, 2021.
- [15] B. Chen, Y. Liu, and *et al.*, “TransAttUNet: Multi-level attention-guided U-Net with transformer for medical image segmentation,” *IEEE Transactions on Emerging Topics in Computational Intelligence*, 2023.
- [16] A. Shaker, M. Maaz, and *et al.*, “UNETR++: Delving into efficient and accurate 3D medical image segmentation,” *IEEE Transactions on Medical Imaging*, vol. 43, pp. 3377–3390, 2024.
- [17] A. Lin, B. Chen, and *et al.*, “DS-TransUNet: Dual swin transformer U-Net for medical image segmentation,” *IEEE Transactions on Instrumentation and Measurement*, vol. 71, pp. 1–15, 2022.
- [18] M. Beck, K. Pöppel, and *et al.*, “xLSTM: Extended Long Short-Term Memory,” *arXiv preprint arXiv:2405.04517*, 2024.
- [19] B. Alkin, M. Beck, and *et al.*, “Vision-LSTM: xLSTM as generic vision backbone,” *arXiv preprint arXiv:2406.04303*, 2024.
- [20] M. M. Rahman, S. Shokouhmand, and *et al.*, “MIST: Medical Image Segmentation Transformer with Convolutional Attention Mixing (CAM) decoder,” in *Proceedings of the IEEE/CVF Winter Conference on Applications of Computer Vision*, pp. 404–413, 2024.
- [21] X. Yan, H. Tang, and *et al.*, “After-UNet: Axial fusion transformer U-Net for medical image segmentation,” in *Proceedings of the IEEE/CVF Winter Conference on Applications of Computer Vision*, pp. 3971–3981, 2022.
- [22] P. Dutta and S. Mitra, “Efficient global-context driven volumetric segmentation of abdominal images,” in *2023 IEEE International Conference on Bioinformatics and Biomedicine (BIBM)*, pp. 1880–1885, 2023.
- [23] P. Dutta and S. Mitra, “Full-scale deeply supervised attention network for segmenting COVID-19 lesions,” in *Proceedings of 20th International Symposium on Biomedical Imaging (ISBI)*, pp. 1–4, IEEE, 2023.
- [24] B. Landman, Z. Xu, J. Igelsias, M. Styner, T. Langerak, and A. Klein, “Miccai multi-atlas labeling beyond the cranial vault—workshop and challenge,” in *Proc. MICCAI Multi-Atlas Labeling Beyond Cranial Vault—Workshop Challenge*, vol. 5, p. 12, 2015.
- [25] N. C. Codella, D. Gutman, and *et al.*, “Skin lesion analysis toward melanoma detection: A challenge at the 2017 International Symposium on Biomedical Imaging (ISBI), hosted by the International Skin Imaging Collaboration (ISIC),” in *Proceedings of the IEEE 15th International Symposium on Biomedical Imaging (ISBI)*, pp. 168–172, IEEE, 2018.
- [26] O. Bernard, A. Lalande, and *et al.*, “Deep learning techniques for automatic MRI cardiac multi-structures segmentation and diagnosis: Is the problem solved?,” *IEEE Transactions on Medical Imaging*, vol. 37, pp. 2514–2525, 2018.

- [27] R. Azad, A. Kazerouni, B. Azad, E. Khodapanah Aghdam, Y. Velichko, U. Bagci, and D. Merhof, “Laplacian-former: Overcoming the limitations of vision transformers in local texture detection,” in *International Conference on Medical Image Computing and Computer-Assisted Intervention*, pp. 736–746, Springer, 2023.
- [28] H. Wang, P. Cao, J. Wang, and O. R. Zaiane, “Uctransnet: rethinking the skip connections in u-net from a channel-wise perspective with transformer,” in *Proceedings of the AAAI conference on artificial intelligence*, vol. 36, pp. 2441–2449, 2022.
- [29] H. Wang, S. Xie, L. Lin, Y. Iwamoto, X.-H. Han, Y.-W. Chen, and R. Tong, “Mixed transformer u-net for medical image segmentation,” in *ICASSP 2022-2022 IEEE international conference on acoustics, speech and signal processing (ICASSP)*, pp. 2390–2394, IEEE, 2022.
- [30] J. Liu, H. Yang, and *et al.*, “Swin-UMamba: Mamba-based U-Net with ImageNet-based pretraining,” in *Proceedings of Medical Image Computing and Computer Assisted Intervention – (MICCAI)*, Springer Nature Switzerland, 2024.
- [31] S. Elfving, E. Uchibe, and *et al.*, “Sigmoid-weighted linear units for neural network function approximation in reinforcement learning,” *Neural Networks*, vol. 107, pp. 3–11, 2018.
- [32] S. A. Taghanaki, Y. Zheng, and *et al.*, “Combo loss: Handling input and output imbalance in multi-organ segmentation,” *Computerized Medical Imaging and Graphics*, vol. 75, pp. 24–33, 2019.
- [33] M. Tan and Q. Le, “EfficientNet: Rethinking model scaling for convolutional neural networks,” in *Proceedings of International Conference on Machine Learning (ICML)*, pp. 6105–6114, PMLR, 2019.